rior resolution. Nonimaging sensors may provide advantages over lens-based cameras, because our knowledge of the environment should be limited by the information available from it and not our sensing or computational methods, analog or digital.

References and Notes

1. L. Mandel and E. Wolf, *Optical Coherence and Quantum Optics* (Cambridge Univ. Press, Cambridge, 1995).
2. C. V. Schooneveld, Ed., *Image Formation from Coherence Functions in Astronomy, IAU Colloquium no. 49* (Reidel, Groningen, Netherlands, 1978), vol. 76.
3. G. W. Swenson, *J. Opt. Soc. Am. A* **3**, 1311 (1986).
4. W. H. Carter and E. Wolf, *Opt. Acta* **28**, 227 (1981).
5. A. J. Devaney, *J. Math. Phys.* **20**, 1687 (1979).
6. I. J. LaHaie, *J. Opt. Soc. Am. A* **2**, 35 (1985).
7. J. Rosen and A. Yariv, *Opt. Lett.* **21**, 1803 (1996).
8. A. M. Zarubin, *Opt. Commun.* **100**, 491 (1993).
9. K. Yoshimori *et al.*, *J. Opt. Soc. Am. A* **14**, 3379 (1997).
10. J. D. Armitage and A. Lohmann, *Opt. Acta* **12**, 185 (1965).
11. F. Roddier, paper presented at the Proceedings of the International Astronomical Union Colloquium, Sydney NSW, Australia, 1979.
12. K. Itoh and Y. Ohtsuka, *J. Opt. Soc. Am. A* **3**, 94 (1986).
13. K. Itoh *et al.*, *Jpn. J. Appl. Phys.* **29**, L1561 (1990).
14. H. K. Tuy, *SIAM J. Appl. Math.* **43**, 546 (1983).
15. L. A. Feldkamp *et al.*, *J. Opt. Soc. Am. A* **1**, 612 (1984).
16. D. L. Marks *et al.*, *Appl. Opt.* **38**, 1332 (1999).

17. Supported by the Defense Advanced Research Projects Agency. D.L.M. acknowledges the support of an NSF Graduate Fellowship.

16 February 1999; accepted 19 May 1999

Chiral Magnetic Domain Structures in Ultrathin FePd Films

H. A. Dürr,[1] E. Dudzik,[1,2] S. S. Dhesi,[1] J. B. Goedkoop,[3] G. van der Laan,[1]* M. Belakhovsky,[4] C. Mocuta,[4] A. Marty,[4] Y. Samson[4]

The magnetization profile of magnetically ordered patterns in ultrathin films was determined by circular dichroism in x-ray resonant magnetic scattering (CDXRMS). When this technique was applied to single crystalline iron palladium alloy layers, magnetic flux closure domains were found whose thickness can constitute a large fraction (~25 percent) of the total film.

X-ray reflections only occur when equivalent sites in a crystal are occupied by identical atoms. If the scattering amplitudes of equivalent sites are not the same, then forbidden reflections can occur. These are pronounced in the case of resonant diffraction, where virtual excitations from core to valence states impose the symmetry properties of the electronic and magnetic structure of the material (*1*). For instance, an antiferromagnetic ordering will give a magnetic superlattice with twice the size of the charge distribution. Here, we show how resonant magnetic scattering can be used to study complicated closure domain patterns (Fig. 1).

The domains display a left-right handedness known as chirality. It can be verified that the magnetization direction of each of the bulk domains in Fig. 1 is related to the magnetization of the closure domains right (left) above by a (counter)clockwise quarter-turn rotation in the *yz* plane. This extra symmetry condition should correspond to an additional Bragg condition, leading to an otherwise forbidden reflection. Although the possibility of measuring the long-period magnetic structure by magnetic x-ray scattering was suggested by Blume in 1985 (*2*) and has been successfully applied to magnetic lattice periodicities on an atomic scale (*3*), we demonstrate here the case of magnetic domain structures. Using x-rays with circular polarization, we can make an unambiguous distinction between magnetic profiles with ↑ → ↓ ← ↑ and ↑ ↓ ↑ ↓ domain patterns because only the former has a chiral structure. The observation of circular dichroism in the x-ray resonant magnetic scattering (CDXRMS) signal, *I*—that is, its difference between left and right circularly polarized photons—allows us to recover the phase information that is generally lost in diffraction experiments. We demonstrate that this effect can be directly related to the magnetization profile in the film.

To observe the magnetization directions, we can use the equivalent in the x-ray region of either the Faraday rotation of linearly polarized light or the Kerr effect of elliptically polarized light. An increase in the sensitivity for the valence electron magnetization is obtained by tuning the photon energy to the Fe L_3 edge (wavelength $\lambda = 17.5$ Å), where a $2p$ core electron is excited into an empty, magnetically aligned $3d$ state. This wavelength is of the correct magnitude to be susceptible to the magnetic periodicity of the sample. The scattering signal measured in a diffraction experiment, $I \propto |\Sigma_n \exp(i\mathbf{q}\cdot\mathbf{r}_n) f_n|^2$ (where $\mathbf{q}$ is the photon wave vector transferred in the scattering process), is the square of the modulus of the sum over all lattice sites, $\mathbf{r}_n$, of the scattering amplitudes, f_n, weighted by a phase factor (*4*). Hannon *et al.* (*5*) showed that the resonant electrical dipole scattering amplitude can be written as

$$f_n = \hat{\mathbf{e}}' \cdot \hat{\mathbf{e}}\, F_n^{(0)} - i(\hat{\mathbf{e}}' \times \hat{\mathbf{e}}) \cdot \hat{\mathbf{M}}_n F_n^{(1)} + (\hat{\mathbf{e}}' \cdot \hat{\mathbf{M}}_n)(\hat{\mathbf{e}} \cdot \hat{\mathbf{M}}_n) F_n^{(2)} \quad (1)$$

where $\hat{\mathbf{e}}$ and $\hat{\mathbf{e}}'$ are the polarization vectors of the incident and scattered x-rays, respectively, and $\hat{\mathbf{M}}_n$ is the unit vector along the magnetization direction in the sample. The complex factors F_n describe the atomic resonant excitation and decay processes, and they can be expanded in terms of multipole moments of the ground state (*6*). The first term in Eq. 1 is due to scattering from the Fe charge distribution, whereas the latter two terms are purely magnetic scattering contributions. In the following we use the second term in Eq. 1 to reconstruct the magnetization profile of the film. The difficulty with this is that usually the absolute magnitude of the complex factors F_n is not very well known and can only be obtained directly under certain conditions, such as for multilayered samples (*7*, *8*). However, the case of regular domain patterns results in an elegant way to separate the three scattering contributions in Eq. 1. The lateral domain periodicity leads to purely magnetic superstructure scattering peaks located symmetrically around the specularly reflected x-ray beam. For structurally well-ordered films with smooth interfaces, the charge scattering term in Eq. 1 contributes only to the specular peak. The two magnetic terms are linear and quadratic in $\hat{\mathbf{M}}_n$ and cause magnetic peaks at wave vectors $\pm\tau$ and $\pm 2\tau$, respectively (2pi/τ is the domain periodicity) (*3*–*5*).

To assess the scattering from the individual domains in Fig. 1B, we must determine the scattering cross sections for the x-ray polarization components σ and π that are perpendicular and parallel to the scattering plane, respectively (*9*). For the scattering geometry used (Fig. 2A) and concentrating on the second term in Eq. 1, there are mainly two scattering paths producing π-polarized scattered light (*4*). For the bulk domains, $\hat{\mathbf{M}}_n$ is perpendicular to the film and σ-polarized incident radiation experiences a Faraday rota-

[1]Daresbury Laboratory, Magnetic Spectroscopy Group, Warrington WA4 4AD, UK. [2]University of York, York YO1 5DD, UK. [3]University of Amsterdam, Valckenierstraat 65, NL 1018 XE Amsterdam, Netherlands. [4]CEA/Grenoble, Service de Physique des Matériaux et Microstructures, 17 rue des Martyrs, 38054 Grenoble Cedex 9, France.

*To whom correspondence should be addressed. E-mail: g.vanderlaan@dl.ac.uk

tion producing a π component (*7, 8, 10*). The other channel is π-π scattering, leaving the incident π polarization unchanged (*11*). It occurs when $\hat{\mathbf{M}}_n$ has a component perpendicular to the scattering plane, as is the case for the closure domains.

Because bulk and closure domains are located at different lateral positions, the x-rays scattered from them will experience a phase shift of 90° (Fig. 1). Unfortunately, this phase shift between the σ-π and π-π scattering is lost when only linear light polarization is used. However, the phase information can be retrieved with circularly polarized radiation. Left and right circularly polarized light is a combination of σ and π polarizations where the π component is advanced or retarded by a phase shift of 90°, respectively, with respect to the σ polarization. As a consequence, the scattering of circularly polarized x-rays from bulk and closure domains will result in a total phase shift of 0 or 180°, depending on the helicity—that is, there will be either constructive or destructive interference, respectively, between the two scattering channels. This is expected to result in strong intensity changes of the magnetic superstructure peaks with incident light helicity; such changes would imply the existence of closure domains.

For an experimental corroboration we used a FePd film (thickness 400 Å), grown by molecular beam epitaxy onto a MgO(001) substrate and capped with a Pd layer (20 Å) to prevent contamination. The layer was grown by codeposition of Fe and Pd with the sample held at 500 K. This leads to layer-by-layer growth and a single crystalline film, as monitored in situ by reflection high-energy electron diffraction (*12*). A magnetic force microscopy (MFM) image of this sample in the as-grown state is shown in Fig. 1A. The image shows clearly the well-ordered alternating up-and-down magnetic domain pattern that is caused by the competition between a perpendicular magnetocrystalline anisotropy and the in-plane shape anisotropy (*12*). The magnetic state is characterized by magnetic flux lines that are partially outside the sample. However, flux closure in the sample (*13*) might be responsible for the high degree of order visible. Despite the important fundamental and technological implications for ultrathin films, such closure domains with a magnetization direction in the film plane are almost impossible to observe even with imaging techniques capable of sufficient lateral resolution, such as MFM, Lorentz microscopy, or scanning electron microscopy with polarization analysis (SEMPA) (*14*). This is because these techniques often monitor the magnetic stray field outside the sample (as is the case for MFM) and provide hardly any information about the magnetic depth profile within the layer (*12*).

We performed CDXRMS measurements at beamline ID12B of the European Synchrotron Radiation Facility (ESRF) in Grenoble, France. Circularly polarized (92%) x-rays were incident along the stripe domains at a grazing angle Θ that could be varied by rotating the sample around the y axis in the film plane (Fig. 2A). Scattered x-rays were detected by a photodiode mounted behind a rectangular aperture that was scanned along the y direction to select the scattering wave vector, $\mathbf{q}_y$, transferred perpendicular to the stripes. The entire setup was mounted in a vacuum chamber to avoid x-ray absorption by air. CDXRMS scans of the scattering signal measured over four orders of magnitude were taken (Fig. 2B). The spectra taken with opposite light helicities at $\Theta = 12°$ show the first-order ($\mathbf{q}_y = \pm\tau$) and second-order ($\mathbf{q}_y = \pm 2\tau$) magnetic peaks located symmetrically around the specularly reflected x-ray beam. We obtain $\tau = 0.0069$ Å^{-1}, which corresponds to a domain period of 909 Å, in good agreement with the MFM result. The difference spectrum displayed on a linear scale (Fig. 2C) shows that the strong circular di-

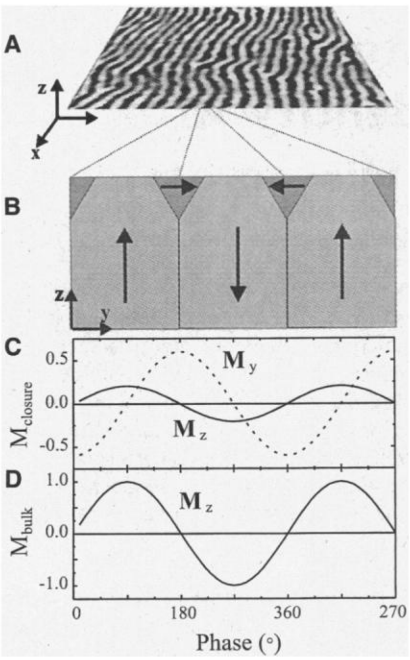

Fig. 1. (**A**) MFM image of a 2 μm by 2 μm area of a 400 Å FePd film grown epitaxially on a MgO(001) substrate. The sample showed a perpendicular magnetic anisotropy quantified by $Q = 0.8$ (Q is the ratio between the magnetic anisotropy and the square of the saturation magnetization). The contrast in the image is due to magnetic domains with flux lines directed upward and downward with respect to the film plane. (**B**) Schematic magnetization profile (*12*) in the *yz* plane of the film. The magnetization directions in the domains are indicated by arrows and illustrate the flux closure in the film. This domain structure is modeled by (**C**) a closure domain layer of effective thickness *t*, and (**D**) the bulk domain layer underneath. In both cases, the magnetization components along the *z* (solid lines) and *y* (dashed line) directions are given as first-order Fourier transforms. Their amplitudes were determined by modeling the experimental data in Fig. 2B. Note that for the closure domain layer (C), *z* and *y* magnetization components occur; this is caused by the extension of the bulk domains into the closure domain layer [see (B)]. The abscissa gives the phase shift, $y\tau$, of the magnetization as the distance in the *y* direction is varied (2pi/τ is the domain periodicity).

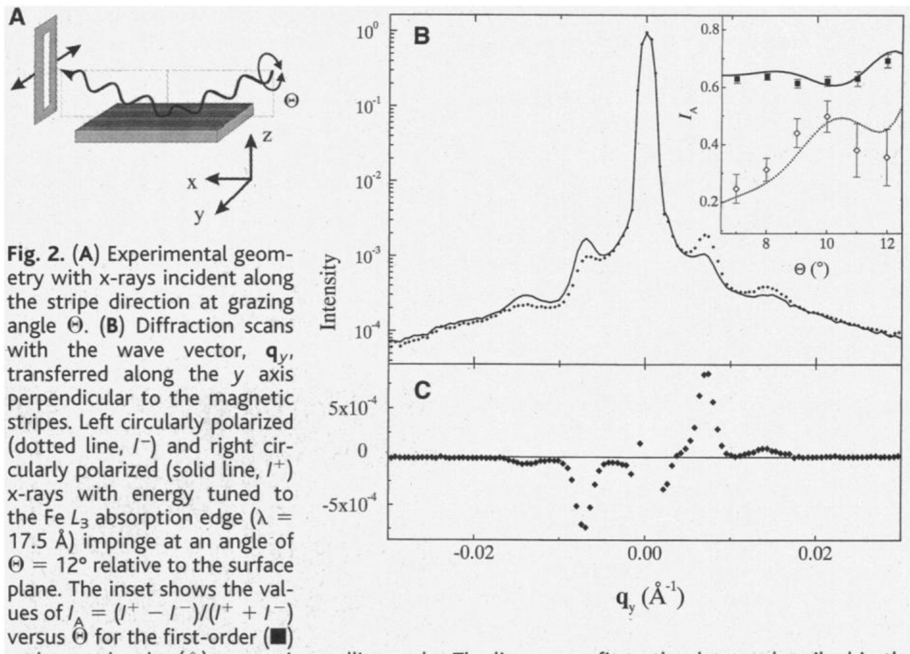

Fig. 2. (**A**) Experimental geometry with x-rays incident along the stripe direction at grazing angle Θ. (**B**) Diffraction scans with the wave vector, $\mathbf{q}_y$, transferred along the y axis perpendicular to the magnetic stripes. Left circularly polarized (dotted line, I^-) and right circularly polarized (solid line, I^+) x-rays with energy tuned to the Fe L_3 absorption edge ($\lambda = 17.5$ Å) impinge at an angle of $\Theta = 12°$ relative to the surface plane. The inset shows the values of $I_A = (I^+ - I^-)/(I^+ + I^-)$ versus Θ for the first-order (■) and second-order (◇) magnetic satellite peaks. The lines are a fit to the data as described in the text. (**C**) Difference signal, $I^+ - I^-$, of the diffraction scans in (B).

chroism in the magnetic peaks reverses sign for negative $\mathbf{q}_y$, as expected from symmetry arguments (*9*). Thus, instead of measuring with opposite light helicities, it would be sufficient to compare the magnetic peak intensities for just one spectrum but with opposite sign of $\mathbf{q}_y$.

To obtain more information about the magnetization depth profile, we measured CDXRMS spectra at different incidence angles. The results are shown in the inset of Fig. 2B, where the ratio of the difference intensity to the sum intensity, $I_A = (I^+ - I^-)/(I^+ + I^-)$, is plotted for the first- and second-order magnetic peaks. Following (*4*), we modeled the measured values taking into account all possible scattering channels according to Eq. 1 (*9*). The periodic lateral modulation of the magnetization was described by Fourier transforms. To simplify the analysis, we approximated the triangular closure domains by sine and cosine waves (Fig. 1C). From the specular reflectivity curve, we determined the x-ray absorption length in FePd at the Fe L_3 edge to be about 400 Å. For the grazing incidence angles used here, it is therefore sufficient to model the film as a semi-infinite slab, thus neglecting the bottom interface where closure domains can also occur.

The I_A signals for both magnetic satellite peaks show strong modulations with Θ. This is caused by a change in the phase relation between the signals from the closure and bulk domain layers as the wave vector perpendicular to the film is varied with Θ, and it provides a direct proof of the existence of closure domains with in-plane magnetization direction. Part of the I_A signals can also be attributed to interference between closure domains and domain walls with a magnetization direction perpendicular to the film within one layer (Fig. 1C); however, this contribution does not vary with Θ.

The amplitudes of the layer magnetization were deduced from modeling the first-order magnetic I_A signals (Fig. 1, C and D). These were representative of closure and bulk domains, respectively. Here, we assumed that the closure domains are distributed uniformly over an effective depth, t, from the surface of the film. The value of t is very sensitive to the angular position of the maxima and minima of $I_A(\Theta)$ in Fig. 2B. We obtain t = 125 Å. The factors $F_n^{(1)}$ in Eq. 1 are mainly proportional to the magnitude of the spin magnetic moment (*6*). Only the first-order Fourier coefficients shown in Fig. 1, C and D, contribute to the first-order magnetic peaks. However, both first-order and third-order Fourier coefficients are important for the second-order magnetic satellite peaks. This increased parameter set causes the fit to be overdetermined for the present limited data range, but this problem could be resolved by obtaining an extended data set in further measurements. The second-order magnetic peaks are interesting because the factors $F_n^{(2)}$ in Eq. 1 contain contributions from other ground-state moments such as the anisotropic spin-orbit coupling. These quantities are of special importance in understanding the magnetocrystalline anisotropy (*15*).

References and Notes

1. P. Carra and B. T. Thole, *Rev. Mod. Phys.* **66**, 1509 (1994).
2. M. Blume, *J. Appl. Phys.* **57**, 3615 (1985).
3. D. Gibbs *et al.*, *Phys. Rev. Lett.* **61**, 1241 (1988).
4. J. P. Hill and D. F. McMorrow, *Acta Crystallogr.* **A52**, 236 (1996).
5. J. P. Hannon, G. T. Trammell, M. Blume, D. Gibbs, *Phys. Rev. Lett.* **61**, 1245 (1988).
6. J. Luo, G. T. Trammell, J. P. Hannon, *ibid.* **71**, 287 (1993).
7. J.-M. Tonnerre *et al.*, *ibid.* **75**, 740 (1995).
8. M. Sacchi *et al.*, *ibid.* **81**, 1521 (1998).
9. For more details, see Science Online (www.sciencemag.org/feature/data/990819.shl).
10. J. B. Kortright, T. M. Rice, R. Carr, *Phys. Rev. B* **51**, 10240 (1995).
11. C. Kao *et al.*, *Phys. Rev. Lett.* **65**, 373 (1990).
12. V. Gehanno, A. Marty, B. Gilles, Y. Samson, *Phys. Rev. B* **55**, 12552 (1997).
13. C. Kittel, *Phys. Rev.* **70**, 965 (1946).
14. C. Stamm *et al.*, *Science* **282**, 449 (1998).
15. G. van der Laan, *Phys. Rev. Lett.* **82**, 640 (1999).

16. We thank K. Larsson, O. Tjernberg, and N. B. Brookes for their help and technical assistance and the ESRF staff for the excellent operational conditions.

11 February 1999; accepted 27 April 1999

Homeotic Transformation of Rhombomere Identity After Localized *Hoxb1* Misexpression

Esther Bell, Richard J. T. Wingate, Andrew Lumsden*

Segmentation of the hindbrain and branchial region is a conserved feature of head development, involving the nested expression of *Hox* genes. Although it is presumed that vertebrate *Hox* genes function as segment identifiers, responsible for mediating registration between elements of diverse embryonic origin, this assumption has remained untested. To assess this, retroviral misexpression was combined with orthotopic grafting in chick embryos to generate a mismatch in *Hox* coding between a specific rhombomere and its corresponding branchial arch. Rhombomere-restricted misexpression of a single gene, *Hoxb1*, resulted in the homeotic transformation of the rhombomere, revealed by reorganization of motor axon projections.

Since the identification of homologs of *Drosophila* homeotic genes in vertebrates, a consensus model for their role during head development has emerged. The hindbrain is subdivided into rhombomeres, whereas adjacent tissues are subdivided into a series of branchial arches. Regional expression of *Hox* genes in the hindbrain is thought to confer identity to rhombomeres (*1*), whereas equivalent expression in the neural crest–derived branchial arches may provide a positional match between the two systems. Motor axons arising within a given pair of rhombomeres project to a single corresponding branchial arch (*2*). Targeted mutation (*3–5*), overexpression (*6, 7*), or manipulation of *Hox* genes by exogenous retinoids (*8*) all support a *Hox* code model (*9*), but none of these approaches can specifically test the assumption that *Hox* genes act as segment identifiers mediating registration between structures along the anteroposterior axis of the head.

One way to address this issue is to gener-

Department of Developmental Neurobiology, King's College London, Guy's Hospital, London SE1 9RT, UK.

*To whom correspondence should be addressed. E-mail: andrew.lumsden@kcl.ac.uk

Fig. 1. Endogenous expression of *Hoxb1* at stages 9 (**A**) and 19 (**B**), and ectopic Hoxb1 expression (brown) in a stage 23 hindbrain after infection with RCAS/*Hoxb1* at stage 3 (**C**).